EDGE ARTICLE

Check for updates

Surface functionalized perovskite nanocrystals: a design strategy for organelle-specific fluorescence lifetime multiplexing†

Anik Kumar Dey, ‡[af] Subhadeep Das, ‡[b] Sharon Mary Jose,[c] Sreejesh Sreedharan,[d] Noufal Kandoth,[e] Surajit Barman,[e] Abhijit Patra, *[b] Amitava Das *[e] and Sumit Kumar Pramanik *[af]

Fluorescent molecules or materials with high photoluminescence quantum yields and stability towards photobleaching are ideally suited for multiplex imaging. Despite complying with such properties, perovskite nanocrystals (Pv-NCs) are rarely used for bioimaging owing to their toxicity and limited stability in aqueous media and towards human physiology. We aim to address these deficiencies by designing core–shell structures with Pv-NCs as the core and surface-engineered silica as the shell (SiO$_2$@Pv-NCs) since silica is recognized as a biologically benign carrier material and is known to be excreted through urine. The post-grafting methodology is adopted for developing [SiO$_2$@Pv-NCs]tpm and [SiO$_2$@Pv-NCs]tsy (tpm: triphenylphosphonium ion, tsy: tosylsulfonamide) for specific imaging of mitochondria and endoplasmic reticulum (ER) of the live HeLa cell, respectively. A subtle difference in their average fluorescence decay times ([SiO$_2$@Pv-NCs]tpm: $^{tpm}\tau_{av}$ = 3.1 ns and [SiO$_2$@Pv-NCs]tsy: $^{tsy}\tau_{av}$ = 2.1 ns) is used for demonstrating a rare example of perovskite nanocrystals in fluorescence lifetime multiplex imaging.

Introduction

Fluorescence lifetime imaging microscopy (FLIM) allows lifetime-multiplexing to simultaneously delineate fluorophores with similar emission spectra but differing lifetimes. Multiplex imaging allows the visualization of the real-time distribution of multiple fluorescent markers simultaneously in different intracellular organelles and microenvironments.[1–3] Simultaneous probing of multiple biomarkers allows for identifying concerted biological pathways that were previously explored only in isolation. Among various challenges, the quest for improved imaging reagents to suit the need for multiplex imaging for diagnostic or theranostic stratification is crucial.[4–6] There are reports on various organelle-specific staining reagents/materials, organic dyes, fluorescent proteins, carbon dots, and plasmonic nanoparticles developed for sensing/ imaging of biomarkers and optical coding.[7,8] Despite such reports, there is a scope for developing organelle-specific fluorescent markers that exhibit high luminescence quantum yield, insignificant photobleaching intricate multistep synthesis and are physiologically benign.[9]

Semiconductor metal halide perovskites are nowadays being used for optoelectronic applications due to their low cost and superior photophysical properties such as large absorption cross sections, high photoluminescence quantum yield (ϕ_{PL}), narrow full width at half-maximum of the characteristic photoluminescence band, long carrier diffusion length, and low trap state density.[10,11] Moreover, they exhibit spectrally tunable luminescence spectra over the entire visible spectral region by compositional alloying and quantum size effects.[12,13] Despite such advantages, reports on the use of any perovskite material in biomedical applications are scarce, as existing halide perovskite nanocrystals lose their structural integrity and luminescence characteristics in the presence of moisture or water vapour.[14,15] Encapsulation into polymer microspheres or deposition of passivation layers onto perovskite quantum dot films, typically, suffers from limitations like the formation of aggregated or bulk materials coated with a passivation layer/ polymer microspheres having an inappropriate size for

[a]CSIR – Central Salt and Marine Chemicals Research Institute, Gijubhai Badheka Marg, Bhavnagar, Gujarat 364002, India. E-mail: sumitpramanik@csmcri.res.in

[b]Department of Chemistry, Indian Institute of Science Education and Research Bhopal, India. E-mail: abhijit@iiserb.ac.in

[c]Department of Biological Sciences, Indian Institute of Science Education and Research, Kolkata, Mohanpur, West Bengal, India

[d]Human Science Research Centre, University of Derby, Kedleston Road, DE22 1GB, UK

[e]Department of Chemical Sciences and Centre for Advanced Functional Materials, Indian Institute of Science Education and Research, Kolkata, West Bengal, India. E-mail: amitava@iiserkol.ac.in

[f]Academy of Scientific and Innovative Research (AcSIR), CSIR-Human Resource Development Centre, Ghaziabad, Uttar Pradesh 201 002, India

† Electronic supplementary information (ESI) available. See DOI: https://doi.org/10.1039/d4sc01447b

‡ Equal contribution.

intracellular uptake, apart from lack of organelle-specificity.[16–19] Hence, functionalized nanomaterials derived from semiconductor metal halide perovskites that retain their structural integrity on cellular internalization and are physiologically benign while possessing high ϕ_{PL}, could be exciting for intracellular imaging. Several synthetic fluorescence-based molecular probes are being used for visualization and monitoring intracellular processes or various subcellular targets (mitochondria, endoplasmic reticulum, lysosomes, nucleus, *etc.*). The use of such molecules does not require genetic engineering of the target cell and is suitable for studies with a wide variety of cell types. However, often broad absorption or emission bands, apart from photobleaching for many of such dyes are not desired for multiplexing applications. Spectrally similar luminescent probes with different organelle affinity, a narrow FWHM (full width at half maximum), a narrow luminescence lifetime distribution, and stability towards photobleaching are ideally suited for observing multiple species simultaneously with high spatiotemporal resolution. Examples of such luminescent probes, beyond synthetic fluorescent organic dye molecules, are scarce in the contemporary literature.[20–23] Recent reports further reveal that the use of perovskite nanocrystals, which generally are stable towards photobleaching and show luminescence bands with narrower FWHM as well as a lifetime distribution, are being used for super-resolution microscopies.[24]

The images obtained through the FLIM technique are typically free from artefacts caused by spatial variations in path length, light scattering, and concentration effects. Moreover, probes with distinct fluorescence lifetimes can be employed for lifetime multiplexing, allowing the possibility of simultaneous detection of subcellular environments and organelles. The distinction of organelles based on the lifetime variation of the probes circumvents the issues related to the spectral crosstalk of multiple probes during luminescence imaging.[25] Probes with distinct fluorescence lifetimes, narrow lifetime distribution, and lifetime differences of ~0.5 ns or more are expected as suitable pairs for multiplexing.[26] However, the lack of suitable luminescence scaffolds and design strategies currently limits the prospects for effective intracellular fluorescence lifetime multiplexing.

In this article, we report a new surface functionalized perovskite material as the core and silica with a water-tolerant passivating surface as the shell ([SiO₂@Pv-NCs]tpm and [SiO₂@Pv-NCs]tsy) to impart the required structural stability towards water for use as an efficient imaging reagent for mitochondria and ER, respectively, in live HeLa cells using confocal laser scanning microscopy (CLSM). Moreover, both reagents showed much-improved stability towards photobleaching. Importantly, time-correlated single photon counting (TCSPC) and FLIM studies revealed that these two reagents exhibited detectable changes in their average fluorescence lifetimes ([SiO₂@Pv-NCs]tpm: $^{tpm}\tau_{av}$ = 3.2 ns and [SiO₂@Pv-NCs]tsy: $^{tsy}\tau_{av}$ = 2.2 ns) when dispersed in water/PBS buffer (pH 7.4), or when localized in a specific organelle ([SiO₂@Pv-NCs]tpm: $^{tpm}\tau_{av}$ = 3.1 ns in mitochondria and [SiO₂@Pv-NCs]tsy: $^{tsy}\tau_{av}$ = 2.1 ns in ER). Importantly, the use of silica as the passivation layer also helps

in the retention of [SiO₂@Pv-NCs]tpm within the mitochondria by efficient physisorption of inner-mitochondrial membrane proteins having thiol and amine functionalities.[27] This enables us to use these two surface-functionalized Pv-NCs for the simultaneous imaging of mitochondria and ER and demonstrate a strategy for employing fluorescence lifetime contrast for the simultaneous imaging of multiple organelles through FLIM.

Results and discussion

Our design strategy allowed us to form a passivating shell of silica on the core CsPbBr₃ perovskite nanocrystals (Pv-NCs) capped with oleic acid (OA) and oleylamine (OAm) following the hot-injection synthesis method. Subsequently, Pv-NCs were subjected to a hydrolysis–condensation reaction to yield SiO₂@Pv-NCs with Pv-NCs as the core and silica-based (SiO₂) surface as the shell. Details of the synthesis of Pv-NCs and the surface passivated SiO₂@Pv-NCs are discussed in the ESI.† For surface passivated SiO₂@Pv-NCs, Pv-NCs were dispersed in toluene, and (3-mercaptopropyl)trimethoxysilane ($C_6H_{15}O_3Si$-SH, MTMS) and Milli-Q water were added to initiate the hydrolysis of MTMS. The higher affinity of Pb^{2+} centres towards sulphide ions would favour the reaction between Pb^{2+}-centres of Pv-NCs and MTMS or its partially hydrolyzed states. This would lead to a coating of SiO₂ layer as the shell on the Pv-NCs, acting as the core, and eventually would generate SiO₂@Pv-NCs with a distinct distribution of pendent sulfhydryl functionalities (*vide infra*) on the shell surface. Recent literature reports also support such a proposition.[28] The SiO₂-surface of this shell structure was further functionalized either with the triphenylphosphonium (tpm) ion ([SiO₂@Pv-NCs]tpm) (tpm: triphenylphosphonium ion) or with the –NH functionalized tosyl (tsy) group ([SiO₂@Pv-NCs]tsy) (Scheme 1). The negative mitochondrial membrane potential ($\Delta\Psi_m \sim -108$ to -180 mV) across the mitochondrial inner membrane favours the inward transport of cationic phosphonium ion localization in the mitochondrial matrix.[29,30] Strong physisorption of the pendant amine/thiol functionalities of the inner mitochondrial membrane proteins on silica surfaces is also expected to favor the retention of the [SiO₂@Pv-NCs]tpm for fixed cell imaging. The sulfonamide functionality effectively binds to the sulfonylurea receptors of adenosine triphosphate (ATP)-dependent potassium channel, over-expressed on the ER, and accounts for the excellent selectivity and affinity for the ER.[31]

As-synthesized Pv-NCs, SiO₂@Pv-NCs, [SiO₂@Pv-NCs]tpm, and [SiO₂@Pv-NCs]tsy were isolated from the crude solution through direct centrifugation, and isolated solids were adequately characterized using various analytical, spectroscopic (UV-vis, fluorescence, and X-ray photoelectron spectroscopy (XPS) studies), powder X-ray diffraction (PXRD), and high-resolution transmission electron microscopy (HRTEM) techniques (Fig. 1 and S1–S13, ESI†). All characterization data of these materials, along with the characterization data of the organelle targeting ligands PHOS-1 and ER-1, are provided in the ESI.† Fig. 1a shows the typical band edge absorption spectrum of Pv-NCs dispersed in toluene with an exciton band around 510 nm and respective narrow-band exciton
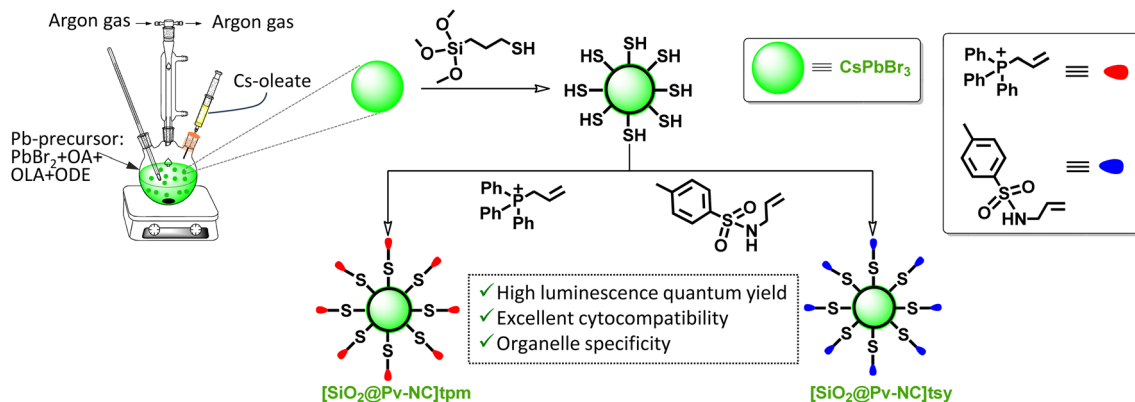
Scheme 1 Schematic diagram for the fabrication of organelle targeting unit-functionalized silica-coated CsPbBr$_3$ perovskite nanocrystals (Pv-NCs), *i.e.*, [SiO$_2$@Pv-NCs]tpm (mitochondria targeting) and [SiO$_2$@Pv-NCs]tsy (endoplasmic reticulum, ER targeting). The synthetic procedure involves the initial fabrication of CsPbBr$_3$ Pv-NCs, followed by the hydrolysis–condensation reaction with a thiol-group-functionalized silica derivative to afford SiO$_2$@Pv-NCs with a distribution of pendant sulfhydryl functionalities on the hybrid Pv-NC surfaces. The subsequent functionalization of SiO$_2$@Pv-NCs with allyltriphenylphosphonium (tpm) and *N*-allyl-4-methylbenzenesulfonamide (tsy) derivative results in mitochondria-specific [SiO$_2$@Pv-NCs]tpm and ER-specific [SiO$_2$@Pv-NCs]tsy, nanocrystals, respectively.

photoluminescence (PL) emission at around 525 nm (FWHM ∼ 20 nm). This green emission with λ_{max} of ∼525 nm is attributed to a band edge-exciton recombination in perovskite CsPbBr$_3$. The PXRD pattern of Pv-NCs shows three strong peaks located at 15.18°, 21.55°, and 30.65°, respectively, for the (100), (110), and (200) planes of the cubic phase of perovskite CsPbBr$_3$ (ICSD no. 00-054-0752, Fig. 1h). This also typically accounts for the green emission observed for Pv-NCs and SiO$_2$@Pv-NCs.

HRTEM studies revealed monodisperse Pv-NC formation as observed after the hot-injection synthesis method (see details in the ESI†). The NCs were distributed in the cubic phase, and the HRTEM showed the well-defined lattice fringes having a lattice constant of 5.8 Å for (100) plane reflection and a uniform size distribution with an average size ∼6.3 ± 0.8 nm (Fig. 1b, c and g). As shown in the inset of Fig. 1c, the HRTEM, FFT pattern endorses the highly crystalline nature of the pristine nanocrystals. The respective powder X-ray diffraction pattern (PXRD)
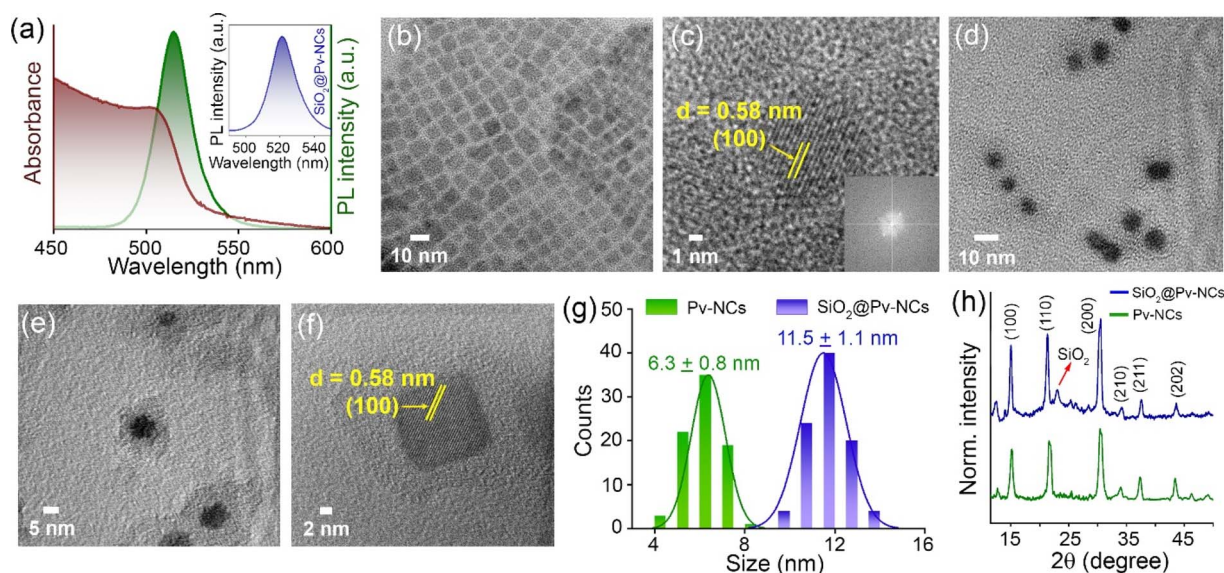

Fig. 1 (a) UV-Vis absorption (brown) and luminescence (green) spectra of as-synthesized Pv-NCs in toluene; inset: luminescence spectra of SiO$_2$@Pv-NCs (blue) in water (λ_{ex} = 488 nm). (b) Transmission electron microscopy (TEM) images of as-prepared Pv-NCs; scale = 10 nm. (c) High-resolution TEM (HRTEM) image of Pv-NCs depicting the *d*-spacing between the (100) lattices (*d* = 0.58 nm); scale = 1 nm; inset: FFT image of Pv-NCs. (d and e) TEM images of as-prepared SiO$_2$@Pv-NCs; for (d) scale = 10 nm, (e) scale = 5 nm. (f) HRTEM image of SiO$_2$@Pv-NCs depicting the *d*-spacing between the (100) lattices (*d* = 0.58 nm); scale = 2 nm. (g) Size distribution of the Pv-NCs (green) and SiO$_2$@Pv-NCs (blue); from this distribution profile, it is clearly observed that the size of SiO$_2$@Pv-NCs increases after silica coating. (h) PXRD patterns of Pv-NCs (green) and SiO$_2$@Pv-NCs (blue) confirm the cubic arrangement of CsPbBr$_3$ perovskite nanocrystals. The broad diffraction pattern at 22° is attributed to the characteristic peak of amorphous SiO$_2$.
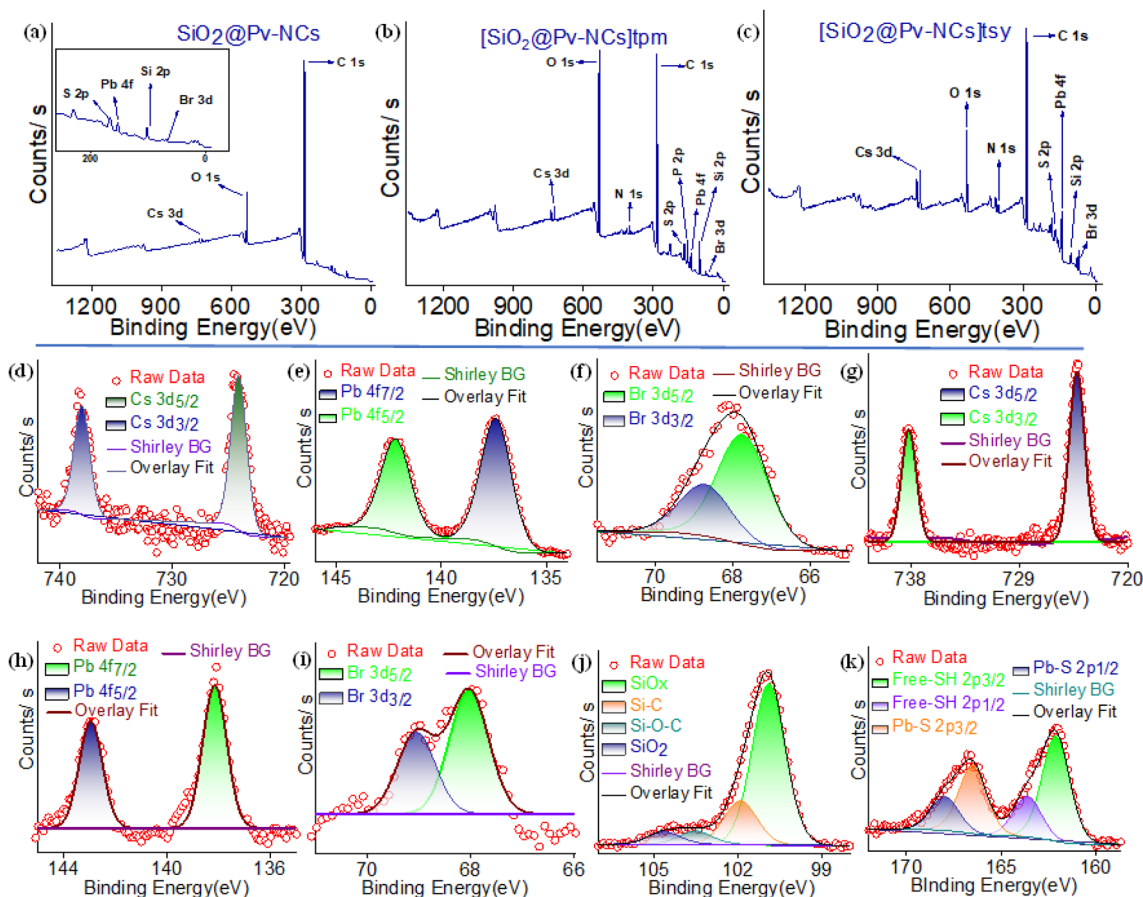
Fig. 2 XPS survey plots of (a) SiO$_2$@Pv-NCs, (b) [SiO$_2$@Pv-NCs]tpm, and (c) [SiO$_2$@Pv-NCs]tsy. High-resolution X-ray photoelectron spectra for Pv-NCs: (d) Cs (3d), (e) Pb (4f), (f) Br (3d), (g) Cs (3d); and for SiO$_2$@Pv-NCs (h) Pb (4f), (i) Br (3d), (j) Si (2p), and (k) S (2p) regions.

shows the peaks properly indexed to the cubic-phase crystal structure of CsPbBr$_3$ ($a = b = c = 5.87$ Å),[32] in line with the HRTEM observation of lattice fringes (Fig. 1c). The surface passivation of Pv-NCs with a narrow layer of silica (SiO$_2$@Pv-NCs) shows a core–shell heterostructure followed by the formation of narrow shell thickness ∼4–5 nm over the perovskite core (Fig. 1d–f). The corresponding lattice reflection at the (100) plane suggests a lattice constant of 5.8 Å. A uniform size distribution with an average dimension of ∼11.5 ± 1.0 nm was evaluated through HRTEM analysis (Fig. 1g).

The PXRD pattern for SiO$_2$@Pv-NCs shows a broad peak between 15° and 35° (Fig. 1h), signifying the presence of amorphous silica.[33] The Fourier-transform infrared (FTIR) spectrum (Fig. S1, ESI†) shows symmetric stretching vibration and asymmetric vibration of (Si–O–Si) at around 804 and 1115 cm^{-1}, respectively.[34] After reaction with tpm, the zeta (ξ) potential for [SiO$_2$@Pv-NCs]tpm (+12.1 mV) was found to change when compared with that for SiO$_2$@Pv-NCs (+23.8 mV), while that for [SiO$_2$@Pv-NCs]tsy was evaluated as +1.2 mV (Fig. S4, ESI†).

The full-scan X-ray photoelectron spectroscopy (XPS) spectrum of the SiO$_2$@Pv-NCs, with signals identified for Cs, Br, Pb, Si, O, and S, is shown in Fig. 2a. Peaks anticipated for each component of Pv-NCs and SiO$_2$@Pv-NCs could be identified.

The high-resolution XPS spectrum revealed additional details of SiO$_2$@Pv-NC formation. For pristine Pv-NCs, the elements Cs, Pb, and Br show similar binding energy peaks to those reported for CsPbBr$_3$ (Fig. 2b and c). In the case of SiO$_2$@Pv-NCs, the Cs 3d peaks split into 3d$_{3/2}$ and 3d$_{5/2}$ at respective peaks of 738.2 eV and 724.2 eV, respectively (Fig. 2d). Further, the Pb 4f orbitals deconvoluted into 4f$_{5/2}$ and 4f$_{7/2}$ orbitals at respective peaks of 142.9 eV and 138.1 eV (Fig. 2e). The emergence of peaks at 166.6 eV and 168 eV represents the formation of Pb–S bond (Fig. 2k).[35] The high-resolution XPS spectrum of the S 4p region supports the presence of the Pb–S bonding in SiO$_2$@Pv-NCs along with free sulfhydryl moiety: peaks at 166.6 eV and 168.0 eV corresponding to 2p$_{3/2}$ and 2p$_{1/2}$ states of the Pb–S bond, respectively (Fig. 2k). Along with these, peaks at 162.1 eV and 163.7 eV originate from 2p$_{3/2}$ and 2p$_{1/2}$ states of free –SH. These suggest a distinct distribution of the free sulfhydryl functionality on the shell surface of the SiO$_2$@Pv-NCs (shell@-core) hybrid. Surfaces of the shell@core hybrid, SiO$_2$@Pv-NCs were further functionalized either with tpm ([SiO$_2$@Pv-NCs] tpm) or with tsy ([SiO$_2$@Pv-NCs]tsy) by exploiting the preferential reaction between the nucleophilic sulfhydryl functionalities of SiO$_2$@Pv-NCs and the respective olefinic functionalities.[18] Surface charge and XPS spectra analysis of [SiO$_2$@Pv-NCs]tpm
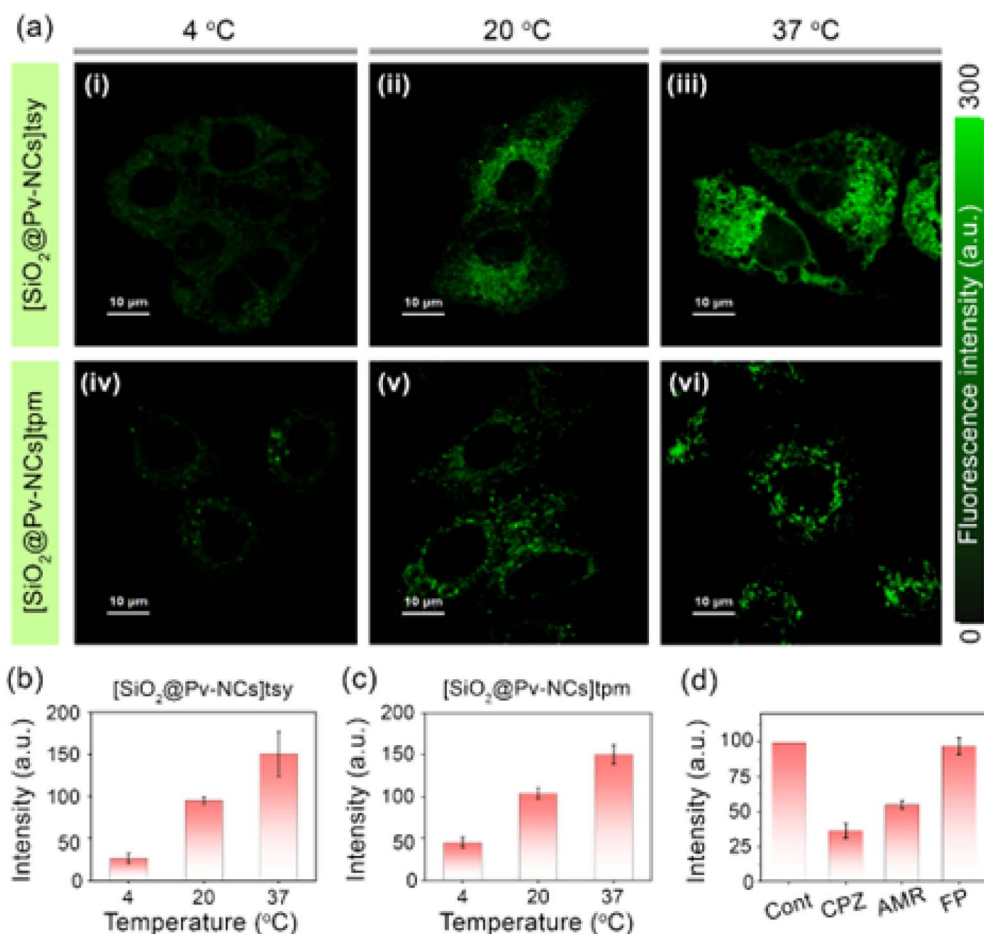
Fig. 3 (a) Temperature-dependent cellular uptake of surface functionalized Pv-NCs (λ_{ex} = 470 nm, λ_{em} = 488–800 nm, conc. $\sim 5 \times 10^{-4}$ mg mL^{-1}) by HeLa cells; confocal laser scanning microscopy (CLSM) images of HeLa cells incubated with (i–iii) [SiO$_2$@Pv-NCs]tsy and (iv–vi) [SiO$_2$@Pv-NCs]tpm. HeLa cells were incubated with the nanocrystals at (i and iv) 4 °C, (ii and v) 20 °C, and (iii and vi) 37 °C for 30 min; scale bar = 10 μm. A common intensity scale for [SiO$_2$@Pv-NCs]tsy and [SiO$_2$@Pv-NCs]tpm is also presented. Intracellular fluorescence intensity variation of cells treated with (b) [SiO$_2$@Pv-NCs]tsy and (c) [SiO$_2$@Pv-NCs]tpm at different temperatures; the bar diagrams are plotted as mean ± standard deviation (three independent measurements). (d) Effect of the endocytic inhibitor on the internalization of nanocrystals; HeLa cells were pre-treated with chlorpromazine (CPZ, 5 μg mL^{-1}), amiloride (AMR, 40 μM), and filipin (FP, 1 μg mL^{-1}) in serum-free medium for 2 h, and then treated with nanocrystals at 37 °C. The cells treated with nanocrystals without inhibitor treatment are considered as control (cont.), and its uptake is expressed as 100%; λ_{ex} = 488 nm, λ_{em} = 515 nm.

and [SiO$_2$@Pv-NCs]tsy are provided in Fig. S4† and 2b, c, respectively (Fig. S4, S6 and S7, ESI†).

The full-scan XPS spectra of [SiO$_2$@Pv-NCs]tpm and [SiO$_2$@Pv-NCs]tsy were recorded (Fig. S6 and S7, ESI†) as a part of the characterization. The high-resolution XPS spectrum for [SiO$_2$@Pv-NCs]tpm shows all the anticipated peaks for Pb 4f$_{5/2}$ and 4f$_{7/2}$ and S 4p regions, apart from additional peaks at 138.6 and 139.3 eV, indicating the presence of the phosphorus (2p$_{3/2}$ and 2p$_{1/2}$) element of the triphenylphosphonium ion. Also, additional peaks at 284.8 eV and 286.3 eV further confirm the presence of C=C (benzene) and C–S (S 4p aliphatic) at the phosphonium moiety in [SiO$_2$@Pv-NCs]tpm. For [SiO$_2$@Pv-NCs] tsy, additional peaks at 168.4 eV, 167.6 eV, 163.9 eV, 163.1 eV, and 284.8 eV were attributed to 2p$_{1/2}$ and 2p$_{3/2}$ states of S–O, 2p$_{1/2}$ and 2p$_{3/2}$ states of S–C, and C=C (benzene), respectively. This also confirms the presence of the post-grafting of the tosyl group in [SiO$_2$@Pv-NCs]tsy.

The luminescence spectra and the time-resolved decay of Pv-NCs and SiO$_2$@Pv-NCs showed good structural integrity of NCs in toluene and Milli-Q water, respectively (Fig. S9, ESI†). The luminescence quantum yields (LQY, ESI†) were evaluated for Pv-NCs (70%; dispersed in dry toluene) and SiO$_2$@Pv-NCs (15%; dispersed in Milli-Q water). Importantly, the relative luminescence intensity of the pristine nanocrystals (Pv-NCs) dispersed in Milli-Q water was found to decrease rapidly to zero (Fig. S8, ESI†), indicating loss of structural integrity in water. Whereas the analogous experiments with SiO$_2$@Pv-NCs showed 15% QY. The luminescence intensity was retained even after storing in water for over 8 weeks, and LQY was found to be 11%. The fitting of lifetime decay of Pv-NCs in dry toluene results in a multi-exponential decay (τ_{av} = 15.2 ns, Fig. S9, ESI†). Also, a multi-exponential decay profile for SiO$_2$@Pv-NCs (τ_{av} = 14.3 ns) was observed in Milli-Q water (Fig. S9, ESI†). Subcellular targeting of nanoparticles as luminescent markers for
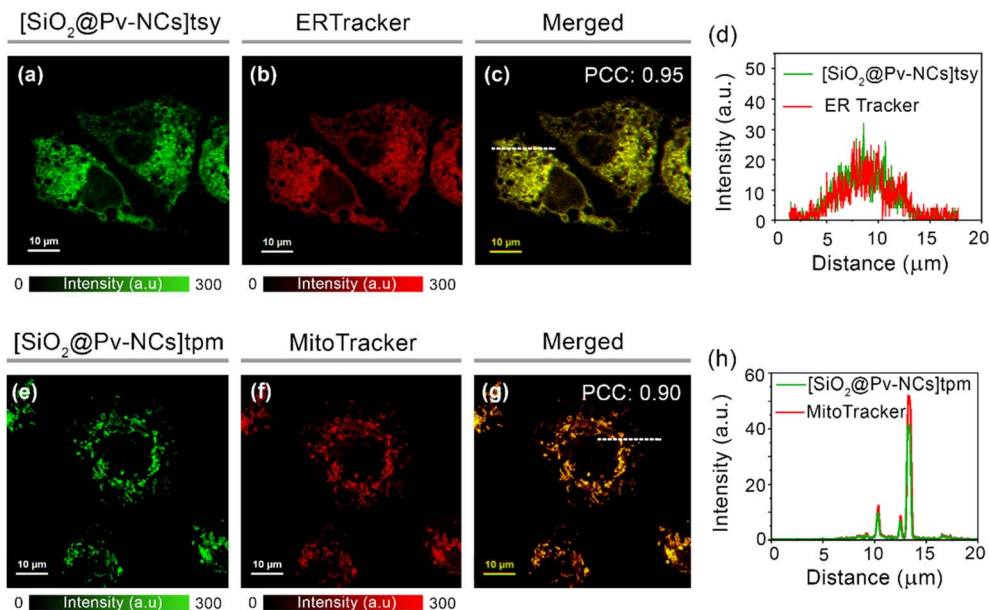
Fig. 4 Intracellular colocalization studies using confocal laser scanning microscopy (CLSM) of live HeLa cells incubated with (a) [SiO$_2$@Pv-NCs]tsy (λ_{ex} = 470 nm, λ_{em} = 500–540 nm, conc.: 5 × 10^{-4} mg mL^{-1}), (b) ERTracker™ Red (λ_{ex} = 640 nm, λ_{em} = 650–690 nm, 0.5 μM), (c) merged image of (a) and (b) indicates ER-targeting ability of [SiO$_2$@Pv-NCs]tsy (Pearson's colocalization coefficient, PCC: 0.95), (e) [SiO$_2$@Pv-NCs]tpm (λ_{ex} = 470 nm, λ_{em} = 500–540 nm, conc.: 5 × 10^{-4} mg mL^{-1}), (f) MitoTracker™ Deep Red (λ_{ex} = 640 nm, λ_{em} = 650–690 nm, conc.: 0.5 μM), (g) merged image of (e) and (f) indicates mitochondria-targeting ability of [SiO$_2$@Pv-NCs]tpm (PCC: 0.90); scale = 10 μm. Common intensity scales are also provided for the fluorescence images. Intracellular intensity profiles of (d) [SiO$_2$@Pv-NCs]tsy and ERTracker, and (h) [SiO$_2$@Pv-NCs]tpm and MitoTracker for the dotted white line depicted in the images (c) and (g) ascertain the endoplasmic reticulum and mitochondria targeting ability of the nanocrystals, respectively.

intracellular imaging is typically achieved through functionalization of the nanoparticle surfaces with organelle/tissue-specific moiety. We followed this methodology to functionalize the silica surfaces of the shell part of SiO$_2$@Pv-NCs (shell@core structure) either with an appropriate tpm or tsy derivative. High negative potential at the matrix face of the mitochondrial inner membrane favours the preferential localization of the cationic triphenylphosphonium (tpm) derivatives in the mitochondrial matrix against their concentration gradient.[36,37] Integrating the methyl sulphonamide moiety within the molecular structure for [SiO$_2$@Pv-NCs]tsy, we have designed a luminescent probe that preferentially accumulates in the ER by binding to sulfonylurea, the sulphonamide receptor, which is abundant on the cytosolic face, as well as the lumen of the ER membrane.[38,39]

UV-Vis spectra and PL decay traces for [SiO$_2$@Pv-NCs]tpm and [SiO$_2$@Pv-NCs]tsy in Milli-Q water, were evaluated using TCSPC experiments (λ_{ex}: 470 nm and λ_{em}: 520 nm; Fig. S5 and S10–S13, ESI†). Biexponential decay kinetics were observed, and τ_{av} for was evaluated ($^{tpm}\tau_{av}$ for [SiO$_2$@Pv-NCs]tpm: 3.2 ns and $^{tsy}\tau_{av}$ for [SiO$_2$@Pv-NCs]tsy: 2.2 ns, Fig. S10 and S12, ESI†). Presumably, the ability of the sulfonamide functionality to participate in hydrogen bonding and undergo effective solvation in an aqueous medium has been attributed to a slightly lower value for $^{tsy}\tau_{av}$. The concentration-dependent studies confirmed that the average fluorescence lifetime of these probes was nominally affected by the nanocrystal concentration, and

thus these probes are suitable for fluorescence lifetime imaging microscopy (Fig. S11†).[40,41]

The stability of the functionalized Pv-NCs ([SiO$_2$@Pv-NCs]tpm and [SiO$_2$@Pv-NCs]tsy) in cell culture media was also ensured following the literature procedure.[42] No change in absorbances was observed when [SiO$_2$@Pv-NCs]tpm and [SiO$_2$@Pv-NCs]tsy were incubated with cell culture media (Fig. S14b, ESI†). Cell viability and phototoxicity assays are important tools for screening and assessing the response of the cells against a drug or a chemical agent. The cell viability studies were performed to check the influences that [SiO$_2$@Pv-NCs]tpm and [SiO$_2$@Pv-NCs]tsy could have on any live cells. We adopted a colourimetric assay using 3-[4,5-dimethylthiazol-2-yl]-2,5 diphenyl tetrazolium bromide (MTT) as the biochemical marker to determine the metabolic activity of the live HeLa cells when incubated in the presence of [SiO$_2$@Pv-NCs]tpm and [SiO$_2$@Pv-NCs]tsy. Details of the MTT assay studies are provided in the ESI section (Fig. S15a, ESI†). The cells were left to incubate for 24 or 48 h in the incubator using 5 × 10^{-4} mg mL^{-1} or 10 × 10^{-4} mg mL^{-1} of [SiO$_2$@Pv-NCs]tpm or [SiO$_2$@Pv-NCs]tsy. For the control experiment, analogous studies were performed in the absence of any modified Pv-NCs. Studies for an extended period (48 h) with higher concentration (10 × 10^{-4} mg mL^{-1}) of [SiO$_2$@Pv-NCs]tpm or [SiO$_2$@Pv-NCs]tsy were performed. MTT assay studies revealed that viability levels in treated HeLa cells remained practically unaffected when compared to a control group (Fig. S15a, ESI†). Indeed, no decrease below 94% was detected even on incubation with different concentrations (10
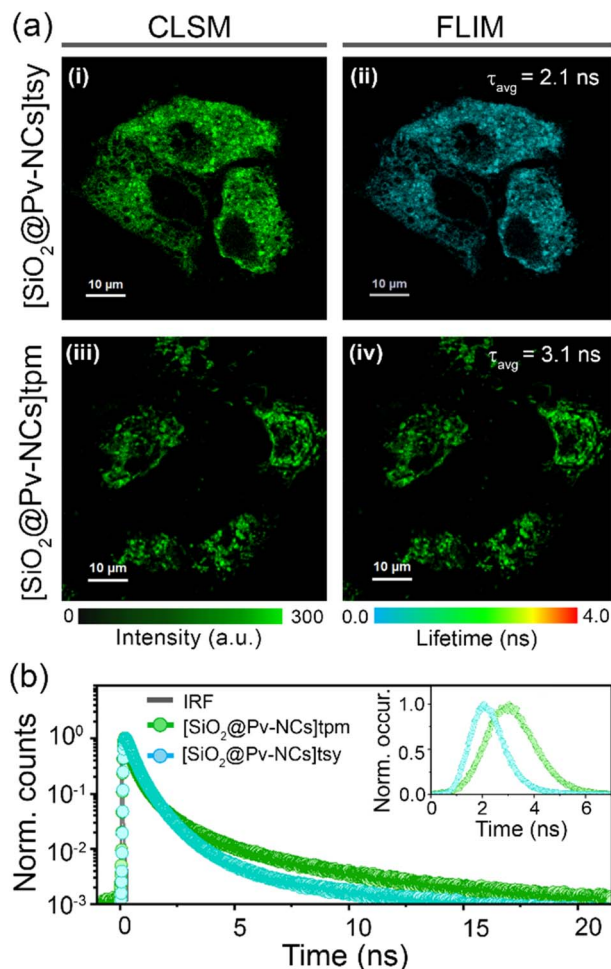
Fig. 5 (a) Images of live HeLa cells incubated with (i and ii) [SiO$_2$@Pv-NCs]tsy and (iii and iv) [SiO$_2$@Pv-NCs]tpm; (i and iii) confocal laser scanning microscopy (CLSM) and (ii and iv) fluorescence lifetime imaging microscopy (FLIM) images (λ_{ex} = 470 nm, λ_{em} = 488–800 nm); scale = 10 μm. A common intensity scale for CLSM and a lifetime scale for FLIM images are shown. (b) Intracellular fluorescence decay curves of HeLa cells incubated with [SiO$_2$@Pv-NCs]tsy (cyan) and [SiO$_2$@Pv-NCs]tpm (green); inset: intracellular lifetime histograms of [SiO$_2$@Pv-NCs]tsy (cyan) and [SiO$_2$@Pv-NCs]tpm (green).

mg mL^{-1}) of [SiO$_2$@Pv-NCs]tpm or [SiO$_2$@Pv-NCs]tsy up to 48 h (Fig. S15a, ESI†). Additionally, for light irradiation (400 nm LED, flux: 80.81 lm) up to 150 min with 100 μg mL^{-1} of SiO$_2$@Pv-NCs, no cell death was observed (Fig. S15b, ESI†). This confirms that [SiO$_2$@Pv-NCs]tpm and [SiO$_2$@Pv-NCs]tsy are biocompatible and show minimal toxicity towards live HeLa cells. Thus, these two reagents could be suitable for biomedical applications.

Next, to optimize the incubation period for imaging studies and to check the specific localization of the probes, time-dependent imaging studies were performed. Confocal laser scanning microscopy (CLSM) images revealed punctate patterns at the initial stages of incubation, which resembled endosome-trapped nanocrystals (Fig. S16, ESI†).[43] This observation intrigued us to check the cellular internalization mechanism for the surface-functionalized nanocrystals (Fig. 3). Endocytosis, an energy-dependent process, is typical for various cells to

communicate with the biological environments and is known to be the dominant pathway for the internalization of nano-particles.[43] To confirm the endocytosis-mediated cellular uptake, the temperature-dependent uptake studies were performed at 37 °C, 20 °C, and 4 °C (Fig. 3). A significant reduction in cellular uptake has been observed at 20 °C and 4 °C, with the fluorescence intensity reduced 25–35% at 20 °C and 65–80% at 4 °C as compared to that observed at 37 °C (Fig. 3a–c). These results suggest that an energy-dependent endocytic process could be the preferred pathway for up to about 75% of NC uptake, while physical diffusion or adhesion presumably contributes to the remaining uptake of the NCs. The reduced fluorescence intensities of the nanocrystals for only ~25–35% at 20 °C could be attributed to the concentration used, as at higher concentrations, the cellular uptake *via* the endocytic pathway is known to be enhanced.[44] Further, to clarify their detailed cellular uptake pathways, the interaction between NCs and cell membranes has been examined by treating the cells with various chemical inhibitors for clathrin-mediated endocytosis, caveolae-mediated endocytosis, and macropinocytosis. The inhibition of clathrin-mediated endocytosis was investigated by using the drug chlorpromazine, which causes clathrin to accumulate in late endosomes, thereby inhibiting coated pit endo-cytosis.[45,46] The cellular uptake of the nanocrystals was reduced by ~65%, compared with the control, indicating that clathrin-mediated endocytosis could be involved. Similarly, amiloride is known to inhibit Na$^+$/H$^+$ exchange, which is required for micropinocytosis.[47] Analogous experiments with amiloride caused a decrease in NC uptake by ~45%. For treatment with filipin, an inhibitor of caveolae-mediated transport processes, failed to influence the NC uptake by the HeLa cells. This could be rationalized based on the absence of caveosomes in HeLa cells (Fig. 3d). Taken together, these results suggest that clathrin-mediated endocytosis and macropinocytosis are presumed to be involved in the internalization of the nanocrystals.

Incubation of [SiO$_2$@Pv-NCs]tpm and [SiO$_2$@Pv-NCs]tsy for longer time periods revealed specific organelle patterns (Fig. S16–S23, ESI†). Distinct tubular and sheet-like morphol-ogies of mitochondria and endoplasmic reticulum were observed by staining HeLa cells with [SiO$_2$@Pv-NCs]tpm and [SiO$_2$@Pv-NCs]tsy, respectively (Fig. S17–S22, ESI†). Strategic passivation of the Pv-NCs with a silica layer also offered us the advantage of retention of [SiO$_2$@Pv-NCs]tpm for fixed cell imaging (Fig. S19, ESI†).[30,33,48] The subcellular localization of [SiO$_2$@Pv-NCs]tpm and [SiO$_2$@Pv-NCs]tsy was investigated by co-staining live HeLa cells with functionalized hybrid nano-crystals and commercial probes specific for mitochondria (MitoTracker™ Deep Red: MTR) and ER (ER-Tracker™ Red: ERTR), respectively, due to their minimal spectral crosstalk (Fig. 4). For [SiO$_2$@Pv-NCs]tsy nanocrystals (λ_{ex} = 470 nm, λ_{em} = 500–540 nm), preferential localization at ER was ascertained with the colocalization studies with ERTR (λ_{ex} = 640 nm, λ_{em} = 650–690 nm) using live HeLa cells. High Pearson's coefficient (0.95) confirmed the localization of [SiO$_2$@Pv-NCs]tsy in ER (Fig. 4a–d and S21, ESI†). [SiO$_2$@Pv-NCs]tpm NCs were excited at 470 nm, and their emission was collected at 500 to 540 nm,
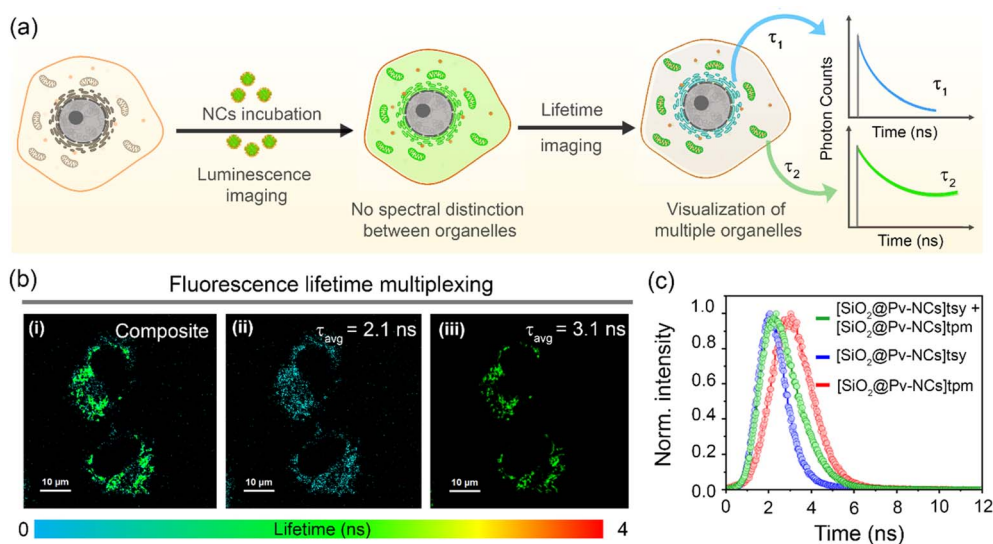
Fig. 6 (a) Schematic representation of intracellular fluorescence lifetime multiplexing employing luminescent nanocrystals (NCs) with variable lifetimes (τ). (b) Fluorescence lifetime multiplexing in HeLa cells co-stained with [SiO$_2$@Pv-NCs]tsy (2×10^{-4} mg mL^{-1}) and [SiO$_2$@Pv-NCs]tpm (2×10^{-4} mg mL^{-1}); representative images indicate (i) composite FLIM image and the separated organelle images with average fluorescence lifetime (τ_{avg}) of (ii) 2.1 ns, and (iii) 3.1 ns. For (b) λ_{ex} = 470 nm, λ_{em} = 488–800 nm, scale = 10 μm. (c) Corresponding intracellular lifetime histograms of HeLa cells incubated with [SiO$_2$@Pv-NCs]tpm (red), [SiO$_2$@Pv-NCs]tsy (blue), and co-incubated with [SiO$_2$@Pv-NCs]tpm and [SiO$_2$@Pv-NCs]tsy (green).

whereas MTR was excited at 640 nm, and the emission was collected in the range of 650–690 nm. An appreciably high Pearson's coefficient (0.90) confirmed the localization of [SiO$_2$@Pv-NCs]tpm in mitochondria (Fig. 4e–h and S22, ESI†). Cross-incubation studies were performed using the mitochondria-targeting nanocrystal ([SiO$_2$@PV-NCs]tpm) with ERTracker™ Red (ERTR) and endoplasmic reticulum-targeting probe ([SiO$_2$@PV-NCs]tsy) with MitoTracker™ Deep Red (Fig. S23, ESI†). The merged images depicted low PCC values for both the cases, thus, the orthogonal targeting ability of the nanocrystals was established (Fig. S23, ESI†). Moreover, both surface functionalized nanocrystals showed significantly improved stabilities towards photobleaching when compared to commercially available dyes (MitoTracker™ Deep Red and ERTracker™ Red used for colocalization studies) under constant laser irradiation (power density: 1.52 W mm^{-2}, Fig. S24–S26, ESI†). The nanocrystals showed excellent long-term imaging ability and could stain the cells for 3 days after single-time incubation (Fig. S28, S29, ESI†). To the best of our knowledge, this is the first demonstration of the use of perovskite materials for organelle-specific localization and imaging.

The organelle-specific localization of functionalized nanocrystals ([SiO$_2$@Pv-NCs]tpm and [SiO$_2$@Pv-NCs]tsy) and the subtle difference in their respective average fluorescence lifetime encouraged us to explore the possibility of fluorescence lifetime imaging microscopy (FLIM) in the mitochondria and ER. First, HeLa cells were incubated separately with [SiO$_2$@Pv-NCs]tpm and [SiO$_2$@Pv-NCs]tsy dispersions in an appropriate culture medium for 30 min at 37 °C. The lifetime maps of [SiO$_2$@Pv-NCs]tpm and [SiO$_2$@Pv-NCs]tsy in live HeLa cells demonstrated a unimodal lifetime distribution (Fig. 5a(ii) and (iv)). Further, the intracellular average fluorescence lifetime for

[SiO$_2$@Pv-NCs]tpm (∼3.1 ns) and [SiO$_2$@Pv-NCs]tsy (∼2.1 ns) showed close resemblance to the respective functionalized Pv-NCs in aqueous medium (Fig. 5a(ii, iv), b and S10, ESI†), indicating no adverse effects on the optical properties of the NCs after mitochondria or endoplasmic reticulum localization, respectively (Fig. 5a).

The similar excitation/emission range, the subtle difference in fluorescence lifetime (∼1 ns), and the distinct organelle targeting ability of these NCs allowed us to investigate the possibility of fluorescence lifetime multiplexing to generate lifetime contrast for simultaneous imaging of multiple organelles using FLIM (Fig. 6a). [SiO$_2$@Pv-NCs]tpm and [SiO$_2$@Pv-NCs]tsy were found to be a suitable pair for lifetime multiplexing of mitochondria and ER, respectively (λ_{ex} = 470 nm, λ_{em} = 488–800 nm). The FLIM images of live HeLa cells co-incubated with [SiO$_2$@Pv-NCs]tpm and [SiO$_2$@Pv-NCs]tsy enable the simultaneous visualization of mitochondria and ER (Fig. 6b). The corresponding fluorescence decay profile and lifetime histogram obtained from the cells incubated with both the nanocrystals indicated the presence of multi-exponential decay with an average fluorescence lifetime of ∼2.4 ns (Fig. 6c and S30, ESI†). However, both the NCs showed a bi-exponential decay profile, and due to the presence of closely aligned decay components, the assignment of mitochondria and ER by choosing individual components could be erroneous. In these circumstances, pattern matching analysis could be more advantageous for multiplexing studies instead of the decay fitting method.[49] Thereafter, distinct organelle patterns of mitochondria,[29] and endoplasmic reticulum,[31] were also successfully deconvoluted using the pattern matching analysis (Fig. 6b(ii, iii) and S30b, ESI†). Thus, the present study presents a generalized strategy for using highly luminescent perovskite nanocrystals with

specific organelle targeting ability and subtle lifetime variations for simultaneous visualization of different organelles in cellular environments.

Conclusion

In summary, we have developed a versatile perovskite material with appropriate functionalization of the water-tolerant passivating shell surfaces for effective organelle-specific internalization and imaging of mitochondria/ER. The use of silica as the passivation shell makes these $SiO_2@Pv$-NCs benign to live HeLa cells and helps in retaining $[SiO_2@Pv$-NCs]tpm within the mitochondrial membrane for fixed cells through interaction with the pendant thiol and amino functionalities of the inner mitochondrial membrane. These hybrid core–shell structures are found to be effective in cellular internalization. Studies confirmed that clathrin-mediated endocytosis is the major and macropinocytosis is the other possible pathway for internalization of these functional nanocrystals. Thus, this methodology demonstrates the relationship between surface chemistry and the subcellular-targeting ability of fluorescent nanocrystals, as well as a way to design pristine perovskite nanocrystals as an efficient imaging probe. The subtle difference in the respective average fluorescence lifetime ($^{tpm}\tau_{av}$ for $[SiO_2@Pv$-NCs]tpm: 3.1 ns and $^{tsy}\tau_{av}$ for $[SiO_2@Pv$-NCs]tsy: 2.1 ns) for these two-surface functionalized Pv-NCs was employed successfully for simultaneous imaging of two different organelles using the FLIM technique. Examples of such perovskite-based NCs that are immune towards the photobleaching process for fluorescence lifetime multiplexing are scarce in the contemporary literature and are likely to open exciting research avenues of biological relevance.

Data availability

All experimental data are available in the ESI.†

Author contributions

Anik Kumar Dey: synthesis of PHOS-1, ER-1, and Pv-NCs and their functionalization, characterization of these compounds/materials. Subhadeep Das: all confocal imaging, FLIM imaging, and the multiplexing studies (using live HeLa cells) reported in the revised manuscript. Sharon Mary Jose: MTT assay data using live HeLa cells presented in the revised manuscript. She also contributed to establishing the conditions for multiplexing using an epifluorescence microscope. Sreejesh Sreedharan: performed initial CLSM images and MTT data reported in the initial version of the manuscript. Noufal Kandoth and Surajit Barman: contributed to recording some of the experimental data that are used for characterization or FLIM studies using epifluorescence microscope. Abhijit Patra: overall supervision of the imaging studies and execution of the biological studies. Sumit Kumar Pramanik and Amitava Das: conceptualization of the problem and overall execution. Anik and Subhadeep equally contributed to the manuscript.

Conflicts of interest

There are no conflicts to declare.

Acknowledgements

References

1 A. Saminathan, M. Zajac, P. Anees and Y. Krishnan, *Nat. Rev. Mater.*, 2022, **7**, 355–371.

2 B. Kepsutlu, V. Wycisk, K. Achazi, S. Kapishnikov, A. J. Pérez-Berná, P. Guttmann, A. Cossmer, E. Pereiro, H. Ewers and M. Ballauff, *ACS Nano*, 2020, **14**, 2248–2264.

3 J. Eng, E. Bucher, Z. Hu, T. Zheng, S. L. Gibbs, K. Chin and J. W. Gray, *Commun. Biol.*, 2022, **5**, 438.

4 J. Liu, Z. Liu, F. Mi, Z. Yao, X. Fang, Y. Wang, Z. Zhao and C. Wu, *Chem. Biomed. Imaging*, 2023, **1**, 550–557.

5 K. Heinzmann, L. M. Carter, J. S. Lewis and E. O. Aboagye, *Nat. Biomed. Eng.*, 2017, **1**, 697–713.

6 Z. Chen and N. G. Ronald, *J. Immunother. Cancer*, 2023, **11**, e006923.

7 H. Singh, K. Tiwari, R. Tiwari, S. K. Pramanik and A. Das, *Chem. Rev.*, 2019, **119**, 11718–11760.

8 J. Li, B. Li, J. Sun, C. Ma, S. Wan, Y. Li, R. Göstl, A. Herrmann, K. Liu and H. Zhang, *Adv. Mater.*, 2020, **32**, 2000964.

9 S. S. Liew, X. Qin, J. Zhou, L. Li, W. Huang and S. Q. Yao, *Angew. Chem., Int. Ed.*, 2021, **60**, 2232–2256.

10 A. Swarnkar, R. Chulliyil, V. K. Ravi, M. Irfanullah, A. Chowdhury and A. Nag, *Angew. Chem., Int. Ed.*, 2015, **127**, 15644–15648.

11 H. Zhang, X. Wang, Q. Liao, Z. Xu, H. Li, L. Zheng and H. Fu, *Adv. Funct. Mater.*, 2017, **27**, 1604382.

12 A. Dey, J. Ye, A. De, E. Debroye, S. K. Ha, E. Bladt, A. S. Kshirsagar, Z. Wang, J. Yin and Y. Wang, *ACS Nano*, 2021, **15**, 10775–10981.

13 X.-S. Hou, H.-S. Wang, B. P. Mugaka, G.-J. Yang and Y. Ding, *Biomater. Sci.*, 2018, **6**, 2786–2797.

14 Y. Huang, Z. Lai, J. Jin, F. Lin, F. Li, L. Lin, D. Tian, Y. Wang, R. Xie and X. Chen, *Small*, 2021, **17**, 2103425.

15 M. Abdi-Jalebi, M. Pazoki, B. Philippe, M. I. Dar, M. Alsari, A. Sadhanala, G. Divitini, R. Imani, S. Lilliu and J. Kullgren, *ACS Nano*, 2018, **12**, 7301–7311.

16 K. Raksha, N. Kandoth, S. Gupta, S. Gupta, S. K. Pramanik and A. Das, *ACS Appl. Mater. Interfaces*, 2022, **15**, 25148–25160.

17 Y. Wang, L. Varadi, A. Trinchi, J. Shen, Y. Zhu, G. Wei and C. Li, *Small*, 2018, **14**, 1803156.

18 S. Seo, S. Shin, E. Kim, S. Jeong, N.-G. Park and H. Shin, *ACS Energy Lett.*, 2021, **6**, 3332–3341.

19 C. Otero-Martínez, N. Fiuza-Maneiro and L. Polavarapu, *ACS Appl. Mater. Interfaces*, 2022, **14**, 34291–34302.

20 E. A. Halabi and R. Weissleder, *J. Am. Chem. Soc.*, 2023, **145**, 8455–8463.

21 E. A. Specht, E. Braselmann and A. E. Palmer, *Annu. Rev. Physiol.*, 2017, **79**, 93–117.

22 S. Pandey and D. Bodas, *Adv. Colloid Interface Sci.*, 2020, **278**, 102137.

23 J.-R. Lin, B. Izar, S. Wang, C. Yapp, S. Mei, P. M. Shah, S. Santagata and P. K. Sorger, *eLife*, 2018, **7**, e31657.

24 B. A. Rosales, M. P. Hanrahan, B. W. Boote, A. J. Rossini, E. A. Smith and J. Vela, *ACS Energy Lett.*, 2017, **2**, 906–914.

25 M. Loidolt-Krueger, *Microsc. Today*, 2023, **31**, 24–31.

26 M. S. Frei, B. Koch, J. Hiblot and K. Johnsson, *ACS Chem. Biol.*, 2022, **17**, 1321–1327.

27 C. Liu, D. L. Steer, H. Song and L. He, *J. Phys. Chem. Lett.*, 2022, **13**, 1609–1616.

28 C. Sun, Y. Zhang, C. Ruan, C. Yin, X. Wang, Y. Wang and W. W. Yu, *Adv. Mater.*, 2016, **28**, 10088–10094.

29 L. D. Zorova, V. A. Popkov, E. Y. Plotnikov, D. N. Silachev, I. B. Pevzner, S. S. Jankauskas, V. A. Babenko, S. D. Zorov, A. V. Balakireva and M. Juhaszova, *Anal. Biochem.*, 2018, **552**, 50–59.

30 S. K. Pramanik, S. Sreedharan, H. Singh, M. Khan, K. Tiwari, A. Shiras, C. Smythe, J. A. Thomas and A. Das, *Bioconjugate Chem.*, 2018, **29**, 3532–3543.

31 X. Tian, F. Yan, J. Zheng, X. Cui, L. Feng, S. Li, L. Jin, T. D. James and X. Ma, *Anal. Chem.*, 2019, **91**, 15840–15845.

32 S. Liu, A. R. DeFilippo, M. Balasubramanian, Z. Liu, S. G. Wang, Y. S. Chen, S. Chariton, V. Prakapenka, X. Luo and L. Zhao, *Adv. Sci.*, 2021, **8**, 2003046.

33 F. Carulli, M. He, F. Cova, A. Erroi, L. Li and S. Brovelli, *ACS Energy Lett.*, 2023, **8**, 1795–1802.

34 H. Sanaeishoar, M. Sabbaghan and F. Mohave, *Microporous Mesoporous Mater.*, 2015, **217**, 219–224.

35 S. Li, D. Lei, W. Ren, X. Guo, S. Wu, Y. Zhu, A. L. Rogach, M. Chhowalla and A. K.-Y. Jen, *Nat. Commun.*, 2020, **11**, 1192.

36 J. Zielonka, J. Joseph, A. Sikora, M. Hardy, O. Ouari, J. Vasquez-Vivar, G. Cheng, M. Lopez and B. Kalyanaraman, *Chem. Rev.*, 2017, **117**, 10043–10120.

37 S. K. Pramanik, S. Sreedharan, R. Tiwari, S. Dutta, N. Kandoth, S. Barman, S. O. Aderinto, S. Chattopadhyay, A. Das and J. A. Thomas, *Chem. Soc. Rev.*, 2022, **51**, 9882–9916.

38 D. Singh, D. Rajput and S. Kanvah, *Chem. Commun.*, 2022, **58**, 2413–2429.

39 H. Xiao, C. Wu, P. Li, W. Gao, W. Zhang, W. Zhang, L. Tong and B. Tang, *Chem. Sci.*, 2017, **8**, 7025–7030.

40 S. Jaiswal, S. Das, S. Kundu, I. Rawal, P. Anand and A. Patra, *J. Mater. Chem. C*, 2022, **10**, 6141–6195.

41 S. Kundu, B. Sk, N. Saha, S. Das, T. K. Dutta, A. Batra, R. S. Tomar and A. Patra, *ACS Mater. Lett.*, 2022, **5**, 27–35.

42 D. Kennedy, V. Gies, A. Jezierski and L. Yang, *SN Appl. Sci.*, 2019, **1**, 1–8.

43 K. Sugano, M. Kansy, P. Artursson, A. Avdeef, S. Bendels, L. Di, G. F. Ecker, B. Faller, H. Fischer and G. Gerebtzoff, *Nat. Rev. Drug Discovery*, 2010, **9**, 597–614.

44 F. Chen, X. Zhang, K. Ma, B. Madajewski, M. Benezra, L. Zhang, E. Phillips, M. Z. Turker, F. Gallazzi and O. Penate-Medina, *ACS Appl. Mater. Interfaces*, 2018, **10**, 4379–4393.

45 S. K. Lai, K. Hida, S. T. Man, C. Chen, C. Machamer, T. A. Schroer and J. Hanes, *Biomaterials*, 2007, **28**, 2876–2884.

46 M. S. de Almeida, E. Susnik, B. Drasler, P. Taladriz-Blanco, A. Petri-Fink and B. Rothen-Rutishauser, *Chem. Soc. Rev.*, 2021, **50**, 5397–5434.

47 L. J. Hewlett, A. R. Prescott and C. Watts, *J. Cell Biol.*, 1994, **124**, 689–703.

48 W. Zheng, S. A. Yamada, S. T. Hung, W. Sun, L. Zhao and M. D. Fayer, *J. Am. Chem. Soc.*, 2020, **142**, 5636–5648.

49 J. C. Thiele, D. A. Helmerich, N. Oleksiievets, R. Tsukanov, E. Butkevich, M. Sauer, O. Nevskyi and J. Enderlein, *ACS Nano*, 2020, **14**, 14190–14200.